


## AUTHOR QUERY FORM

	<p>Journal: Phys. Fluids</p> <p>Article Number: POF24-AR-00236</p>	<p>Please provide your responses and any corrections by annotating this PDF and uploading it to AIP's eProof website as detailed in the Welcome email.</p>
---	--	--

Dear Author,

Below are the queries associated with your article; please answer all of these queries before sending the proof back to AIP.

**Article checklist:** In order to ensure greater accuracy, please check the following and make all necessary corrections before returning your proof.

1. Is the title of your article accurate and spelled correctly?
2. Please check affiliations including spelling, completeness, and correct linking to authors.
3. Did you remember to include acknowledgment of funding, if required, and is it accurate?

Location in article	Query / Remark: click on the Q link to navigate to the appropriate spot in the proof. There, insert your comments as a PDF annotation.
AQ1	Please check that the author names are in the proper order and spelled correctly. Also, please ensure that each author's given and surnames have been correctly identified (given names are highlighted in red and surnames appear in blue).
AQ2	Please note that Kunzelman <i>et al.</i> , 2007 is cited in the text but their corresponding reference is missing in the reference list. Kindly provide the reference in the list or delete its citation from the text.
AQ3	Please update Asghar <i>et al.</i> , with volume number, page number, and year if the article has since been published in print.
AQ4	Please provide page number in Calandrini and Aulisa, 2019, also provide DOI for the same.
AQ5	Please provide volume and page number in Khan <i>et al.</i> , 2023, also provide DOI for the same.
AQ6	The citation for Calandrini and Aulisa, 2018 has been changed to Calandrini and Aulisa, 2019 to match the reference list. Please confirm the change.
	Please confirm ORCID's are accurate. If you wish to add an ORCID for any author that does not have one, you may do so now. For more information on ORCID, see <a href="https://orcid.org/">https://orcid.org/</a> .
	Jongmin Yang - 0009-0002-2043-487X
	Please check and confirm the Funder(s) and Grant Reference Number(s) provided with your submission:
	National Research Foundation of Korea, Award/Contract Number RS-2023-00274580
	National Research Foundation of Korea, Award/Contract Number 2023RIS-009
	Please add any additional funding sources not stated above:

Thank you for your assistance.

# Fluid-structure interaction for mechanical filament valve mimicking a biological leaflet valve

Cite as: Phys. Fluids **36**, 000000 (2024); doi: 10.1063/5.0196671

Submitted: 9 January 2024 · Accepted: 14 February 2024 ·

Published Online: 0 Month 0000



Jongmin Yang (양종민)<sup>a)</sup>

## AFFILIATIONS

Department of Mechanical System Engineering, Jeju National University, 102 Jejudaehak-ro, Jeju-si, Jeju-do 63243, South Korea and Major of Mechanical Engineering, Faculty of Applied Energy System, Jeju National University, 102 Jejudaehak-ro, Jeju-si, Jeju-do 63243, South Korea

<sup>a)</sup>Author to whom correspondence should be addressed: [jmyang@jejunu.ac.kr](mailto:jmyang@jejunu.ac.kr)

## ABSTRACT

The biological leaflet valve is a structure found in blood vessels and the cardiac system, designed to maintain a unidirectional flow within the vessels. Two filaments inspired by the biological leaflet are installed inside the channel, and behavior of two filaments is explored by using immersed boundary method. It is observed that the filaments serve as a valve, maintaining the unidirectional flow inside the channel depending on the length ( $L$ ) and the initial inclined angle ( $\theta$ ) of the filaments. The behavior of the filaments is classified into three modes based on the flow characteristics around the filaments. The pressure and vorticity fields in the vicinity of the filaments are examined to investigate the influence of the surrounding flow on the behavior of filaments. The present study reveals the time sensitivity of valve response, the power consumption, and hydrodynamic efficiency ( $\eta_{V,steady}$ ) of the filament valve, noting that the response speed of the filament valve can vary up to 2.5 times depending on  $L$  and  $\theta$ . The dynamic behavior of the filament valve is analyzed with respect to changes in the properties of the filaments, observing a monotonic decrease in hydrodynamic efficiency with an increase in the bending rigidity ( $\gamma$ ) of the filaments. As a result, the present study will be employed as a cornerstone in the development of a mechanical system that emulate biological structures through biomimetics.

Published under an exclusive license by AIP Publishing. <https://doi.org/10.1063/5.0196671>

## I. INTRODUCTION

In the realm of various issues within the biological fluid flow, hemodynamics encompasses the study of blood flow within the cardiac system and blood vessels from the perspective of fluid mechanics. The Graetz problem, which includes the circular ducts such as blood vessels and channel, has been extensively studied and analyzed due to its significance. Khan and co-workers (2019; 2022) scrutinized the Graetz problem considering the non-Newtonian characteristics of blood. Also, Khan *et al.* (2023a; 2023b) examined the difference between blood flow and Newtonian fluid by assuming blood as a typical viscoplastic fluid. Irregularities in the vascular structure or complex biological structures within vessels cause flow resistance, influencing the behavior of fluid flow within blood vessels. Asghar *et al.* (2023a; 2023b) assumed irregular wavy passages due to Cilia structures and obtained velocity profile and pressure gradient on irregular passages. Additionally, this research also incorporates magnetohydrodynamics (MHD) by considering the non-Newtonian properties and electromagnetic characteristics of blood. Conversely, many research focus on the structural characteristics of the hemodynamic system and their roles in

blood flow rather than issues in non-Newtonian behavior of blood flow. The hemodynamic system, which contains various complex biological structures designed to maintain a unidirectional blood flow, was also characterized by high levels of durability and long-term operational capacity over a lifetime, as noted by Sotiropoulos *et al.* (2016). The structural feature of the hemodynamic system aimed at maintaining a unidirectional blood flow is a valve formed through leaflet or bileaflet structures. The leaflet valve, evolved to regulate blood flow, can be broadly categorized into two types: one controlled by muscle tissue known as chordae tendineae, and the other composed solely of leaflets without muscle attachment. Chordae tendineae-attached leaflet valves were commonly observed in the cardiac system (Kunzelman *et al.*, 2007; Sotiropoulos *et al.*, 2016), while leaflet valves without chordae tendineae were found in vein valves or some portions of the cardiac system (Borazjani, 2013; Calandrini and Aulisa, 2019; and Hajati *et al.*, 2020).

Numerous studies were conducted to examine the fluid dynamic characteristics of chordae tendineae-attached leaflet valves (Pierrakos and Vlachos, 2006; Le and Sotiropoulos, 2013). A significant feature in

leaflet valves was the formation of vortical structures through the fluid–structure interaction, known as vortex rings (Zhang *et al.*, 2019; Zhang and Rival, 2020). The development of these vortex rings was closely related to the development of the incoming jet flow into the mitral valve (Watton *et al.*, 2008). Querzoli *et al.* (2010) detected large-scale coherent structures during diastole and analyzed the interaction between these structures and the incoming jet, revealing that the jet flow formed by the valve disrupts the formation of coherent structures during diastole. Various approaches were made to implement the leaflet valve without chordae tendineae and to compare it with an actual biological leaflet valve. Borazjani (2013) observed that vortical structures formed in mechanical leaflet valves break down into small-scale vortices. Calandrini and Aulisa (2019) noted a decrease in backflow through the leaflet valve with an increase in Young's modulus. Hajati *et al.* (2020) successfully analyzed the fatigue failure of leaflets using von Mises stress with the velocity of blood through the leaflet valve. Due to these characteristics, many attempts had been made to develop mechanical heart valves mimicking leaflet valves (Pierrakos and Vlachos, 2006; Wang *et al.*, 2017), with efforts to analyze them using computational fluid dynamics (Choi *et al.*, 2014; Su *et al.*, 2019; and Lantz *et al.*, 2021). For the analysis of such biological flows, including blood flow through computational fluid dynamics, the implementation of the fluid–structure interaction (FSI) is deemed essential to simulate biological tissues and analyze their interactions with surrounding flows.

Fluid–structure interaction (FSI) is widely used to analyze the fluid flow around various biological tissues with soft body characteristics. Due to these properties, numerous studies using FSI had been conducted to interpret the propulsion mechanisms of various organisms through biomimetics (Park and Sung, 2018; Ryu and Sung, 2019; and Yang *et al.*, 2021). FSI has also been employed for the purpose of analyzing fluid flow within biological tissues. Recently, many studies had applied fluid-flexible body interaction to analyze blood flow within blood vessels (Borazjani, 2013; Calandrini and Aulisa, 2019; and Hajati *et al.*, 2020). Most research on hemodynamic flow through numerical analysis focus on numerically calculating the structure of blood vessels, including leaflets, and analyzing the flow characteristics within these structures. This leads to the elucidation of the vortical structures formed by leaflets and their roles. However, many studies consider only the shape of biological leaflet valves present in blood vessel structures, resulting in relatively limited research on how valve efficiency changes with leaflets of different lengths or inclined angles, as compared to biological valves. From this perspective, the influence of

biological structures such as leaflets on fluid flow is not yet fully understood. Particularly, the changes in fluid flow within blood vessels due to variations in the geometric characteristics of leaflet structures remain an important research topic.

The objective of the present study is to implement the mechanical valve inside a channel flow by installing flexible filaments mimicking the leaflets of a biological leaflet valve without chordae tendineae. Since the fluid in many mechanical systems behaves in the form of Newtonian fluid, the characteristics of non-Newtonian fluid will be disregarded in the present study. A pair of clamped filaments with inclined angles will be installed inside the channel, and the fluid–structure interaction between the filaments and the flow within the channel will be simulated. The penalty immersed boundary method will be employed to analyze the fluid flow within the channel. The biological leaflet valve operates based on the pressure gradient formed in the cardiac system. Hence, the channel flow in the present study will operate in two procedures. First, the channel flow will operate by a fixed scale of favorable pressure gradient until reaching a steady flow regime subsequently. Second, the channel flow will have a backflow by a fixed scale of adverse pressure gradient. Within the second procedure, the filament system will act as a mechanical valve through the deflection of filaments. The study will also analyze the changes in flow characteristics within the channel due to variations in the geometrical characteristics and physical properties of the filaments. The characteristics of the mechanical valve will be determined using the volume flow rate passing through the channel, and valve efficiency will be applied to analyze the efficiency of the mechanical valve based on the properties of the filaments. Furthermore, the vorticity fields and pressure fields in the vicinity of filaments will be examined to analyze the influence of filaments in the mechanical valve. The present study will comprise four sections, including an Introduction. Section II contains the numerical setup for analyzing the fluid–structure interaction and governing equations using the immersed boundary method. Section III discusses the analysis results for the mechanical valve composed of channels and filaments. The summary and conclusion of the present study will be presented in Sec. IV.

## II. PROBLEM FORMULATION

The problem addressed in the present study is composed of a two-dimensional channel flow operating under a pressure gradient and two flexible filaments clamped at the channel wall. This system simplifies the leaflet structure installed inside blood vessels into a filament form, and the overall schematic diagram of this system is shown in Fig. 1. The length of the filament is defined as  $L$ , and the initial inclined

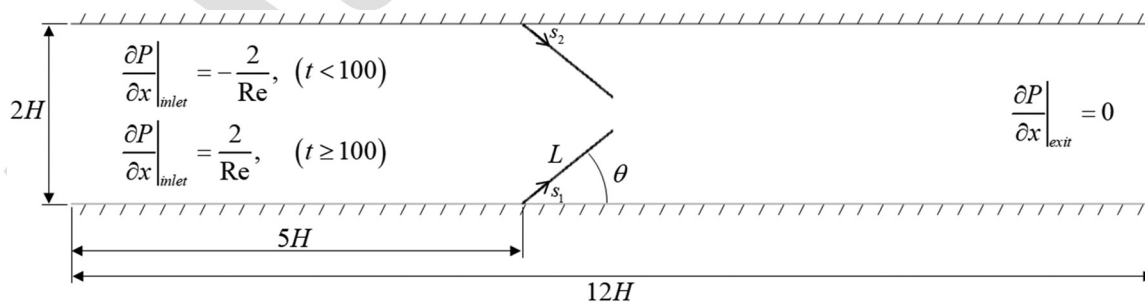


FIG. 1. Schematic diagram of the two clamped filaments within the channel and boundary conditions of the channel.

angle of the filament is defined as  $\theta$ . One end of the filament is clamped to the wall with an inclined angle, while the other end is free to move within the fluid flow. No-slip boundary condition is applied at the wall of the channel, and pressure boundary conditions described in Eq. (1) are imposed at the inlet and outlet of the channel. The initial condition of the flow is quiescent but gradually developed under the influence of a pressure gradient of flow domain. The pressure gradient varies over time, initially operating with a favorable pressure gradient to form a steady-state flow. After the flow reaches a steady-state, the pressure gradient switches to an adverse pressure gradient of the same magnitude as the favorable pressure gradient. If the influence of the filaments is disregarded, the volume flow rate of the streamwise direction gradually decreases under the influence of the adverse pressure gradient, eventually acquiring a negative value. In other words, a phenomenon occurs where the flow direction in the streamwise direction switches, which will be defined as a “backflow” in the present study. Consequently, as the pressure gradient changes over time from a favorable pressure gradient to an adverse pressure gradient, the transition of pressure gradient results in the “backflow” in the channel flow. The time-dependent variation of the non-dimensionalized pressure gradient can be defined in the form of Eq. (1)

$$\begin{aligned} \left. \frac{\partial p}{\partial x} \right|_{\text{inlet}} &= -\frac{2}{\text{Re}} \quad (t < 100), \\ \left. \frac{\partial p}{\partial x} \right|_{\text{inlet}} &= \frac{2}{\text{Re}} \quad (t > 100), \\ \left. \frac{\partial p}{\partial x} \right|_{\text{outlet}} &= 0. \end{aligned} \quad (1)$$

The motion of the filaments can vary depending on the internal pressure changes and the geometric conditions of the filament ( $L, \theta$ ) in the fluid flow. The filaments may exhibit a flapping motion within the flow or remain in a deflected state. The interaction between the fluid flow and the filament, which determines the state of motion of the filament, is obtained using the penalty immersed boundary method.

In the present study, the penalty immersed boundary (IB) method was employed to examine the interaction between fixed filaments and the surrounding flow, following the works of Peskin (2002), Huang *et al.* (2007), Kim and Peskin (2007), and Huang and Sung (2009). In the penalty immersed boundary method, the fluid flow is described by the incompressible Navier–Stokes equations defined on an Eulerian grid, while the motion of the elastic filaments is described by the elastic motion equation defined on a Lagrangian grid. The governing equations that dictate fluid motion are outlined in Eqs. (2) and (3)

$$\begin{aligned} \rho_0 \left( \frac{\partial \mathbf{u}}{\partial t} + \mathbf{u} \cdot \nabla \mathbf{u} \right) &= -\nabla p + \mu \nabla^2 \mathbf{u} + \mathbf{f}, \\ \nabla \cdot \mathbf{u} &= 0, \end{aligned} \quad (2)$$

where  $\mathbf{u} = \{u, v\}$ ,  $p$ , and  $\mu$  denote the velocity vector of fluid motion, pressure, and dynamic viscosity for Newtonian fluid, respectively. Additionally,  $\mathbf{f} = \{f_x, f_y\}$  represents the momentum forcing term to the fluid motion exerted by a flexible body with a no-slip boundary condition. The motion of flexible filaments within the fluid motion is governed by the elastic motion equation, and the form of the governing equation is as presented in Eq. (4)

$$\rho_1 \frac{\partial^2 \mathbf{X}}{\partial t^2} = \frac{\partial}{\partial s} \left( \sigma \frac{\partial \mathbf{X}}{\partial s} \right) - \frac{\partial^2}{\partial s^2} \left( \gamma \frac{\partial^2 \mathbf{X}}{\partial s^2} \right) - \mathbf{F}, \quad (4)$$

where  $\mathbf{X} = \{X(s, t), Y(s, t)\}$  represents the displacement vector of the filament, and  $s$  is a coordinate of the Lagrangian grid formed along the filaments.  $\gamma$  represents the bending rigidity of flexible filaments, and  $\mathbf{F}$  is the momentum forcing term to the flexible body exerted by a fluid motion on the Eulerian grid. In the present work, the non-dimensionalized bending rigidity of  $\gamma = 0.5$  is utilized as a reference value, and it can vary from 0.1 to 0.6 to investigate the influence of bending rigidity on the behavior of filaments. Equations (2)–(4) can be nondimensionalized using corresponding scales for length, velocity, and pressure: length is scaled with the channel’s half-height  $H$ , velocity with the centerline velocity  $U_{CL}$  of the fully developed channel flow, and time is defined by  $T = H/U_{CL}$ . The nondimensional governing equations defined in this manner are presented as Eqs. (5) and (6)

$$\frac{\partial \mathbf{u}}{\partial t} + \mathbf{u} \cdot \nabla \mathbf{u} = -\nabla p + \frac{1}{\text{Re}} \nabla^2 \mathbf{u} + \mathbf{f}, \quad (5)$$

$$\frac{\partial^2 \mathbf{X}}{\partial t^2} = \frac{\partial}{\partial s} \left( \sigma \frac{\partial \mathbf{X}}{\partial s} \right) - \frac{\partial^2}{\partial s^2} \left( \gamma \frac{\partial^2 \mathbf{X}}{\partial s^2} \right) - \mathbf{F}, \quad (6)$$

where  $\text{Re} = \rho_0 U_{CL} H / \mu$  is the Reynolds number. The two ends of the flexible filament are composed of an inclined clamped condition and a free end. The inclined clamped condition, assigned at  $s = 0$ , can be described as follows:

$$X = X_0, \quad \frac{\partial X}{\partial s} = \{\cos \theta \sin \theta\}. \quad (7)$$

Furthermore, the free end condition, assigned at  $s = L$ , can be described as follows:

$$\sigma = 0, \quad \frac{\partial^2 X}{\partial s^2} = 0, \quad \frac{\partial^3 X}{\partial s^3} = 0. \quad (8)$$

The interaction between the fluid and the flexible body in Eulerian and Lagrangian grids can be handled using the Penalty IBM method (Goldstein *et al.*, 1993; Huang *et al.*, 2007). The magnitude of the force generated due to the fluid–flexible body interaction is defined as in Eq. (9)

$$\mathbf{F} = \alpha \int_0^t (\mathbf{U}_{ib} - \mathbf{U}) dt' + \beta (\mathbf{U}_{ib} - \mathbf{U}), \quad (9)$$

where  $\alpha$  and  $\beta$  are set as very large negative constants. In the present study, ( $\alpha = -1.5625 \times 10^6$ ,  $\beta = -78.125$ ) are used to calculate the interaction forces, and these constants are defined and utilized based on the various studies (Shin *et al.*, 2008; Lee *et al.*, 2018; and Wang *et al.*, 2020).  $\mathbf{U}$  represents the velocity vector of the filament defined as  $\mathbf{U} = \frac{d\mathbf{X}}{dt}$ , and  $\mathbf{U}_{ib}$  is defined as the fluid velocity at the immersed boundary obtained through the interpolation method. The relationship between the fluid velocity defined in the Eulerian grid and  $\mathbf{U}_{ib}$  can be defined using the Dirac delta function (Peskin, 2002)

$$\mathbf{U}_{ib} = \int_{\Omega} \mathbf{u}(\mathbf{x}, t) \delta(\mathbf{X}(s, t) - \mathbf{x}) d\mathbf{x}, \quad (10)$$

where  $\Omega$  represents the Eulerian domain used for the interpolation, and  $\mathbf{x}$  denotes the displacement vector of the fluid in the Eulerian grid. Utilizing this relationship, the displacement of the flexible body filament over time can be defined as in Eq. (11)

$$\mathbf{X}_{ib}^{n+1} = \mathbf{X}_{ib}^n + \mathbf{U}_{ib}^{n+1} \Delta t, \quad (11)$$



where the superscript  $n$  denotes the properties of the  $n$ th time step. Conversely, the momentum forcing terms defined in the Lagrangian grid in Eqs. (9)–(11) need to be transformed into the Eulerian grid to be integrated into the fluid governing equations. Therefore, the Eulerian momentum forcing term  $\mathbf{f}$  can be expressed as in Eq. (12) through the Lagrangian forcing term  $\mathbf{F}$  with the Dirac delta function

$$\mathbf{f}(\mathbf{x}, t) = \rho \int_{\Gamma} \mathbf{F}(s, t) \delta(\mathbf{x} - \mathbf{X}(s, t)) d\Gamma, \quad (12)$$

where  $\rho = \rho_1/\rho_0 L$  represents the mass ratio (Eloy *et al.*, 2007). Since the magnitude of the inertial forces of the flexible body is less than for the hydrodynamic forces for general cases, the present study utilized  $\rho = 1.0$  (Daniel and Combes, 2002; Yeh and Alexeev, 2014).

In the present study, the fractional step method is employed to discretize and analyze the governing equation of fluid motion, the Navier–Stokes equation (Kim *et al.*, 2002). The forms of the discretized equations are presented in Eqs. (13) and (14)

$$\frac{\mathbf{u}^{n+1} - \mathbf{u}^n}{\Delta t} + N\mathbf{u}^{n+1} = -Gp^{n+1/2} + \frac{1}{2\text{Re}}(L\mathbf{u}^{n+1} + L\mathbf{u}^n) + \mathbf{f}^n + \mathbf{mbc}, \quad (13)$$

$$D\mathbf{u}^{n+1} = 0 + \mathbf{cbc}, \quad (14)$$

where  $N$ ,  $G$ ,  $L$ , and  $D$  are the linear operators, representing the convective operator, the gradient operator, the Laplacian operator, and the divergence operator, respectively. The boundary conditions for the governing equations are denoted as  $\mathbf{mbc}$  and  $\mathbf{cbc}$ . The Crank–Nicolson scheme for time and the second-order central difference scheme for space are applied for the discretization of the governing equation. Additionally, the velocity and pressure terms were decoupled using the block-upper decomposition with approximate factorization during the discretization process with second-order accuracy (Kim *et al.*, 2002).

In the present study, the channel flow with  $\text{Re} = 100$  and clamped filaments with a nondimensionalized bending rigidity of  $\gamma = 0.5$  are explored. Consequently, a no-slip boundary condition is applied to the top and bottom surfaces of the channel flow. The pressure conditions from Eq. (1) are imposed at the channel inlet and outlet. To examine the influences of mesh resolution in Eulerian and Lagrangian grids, trial calculations are conducted. Figure 2 illustrates the variation in filament displacement with changes in the Eulerian grid resolution and Lagrangian grid resolution. It is observed that a

Lagrangian grid resolution of  $\Delta s/L$  smaller than  $1/64$  does not affect the analysis results, and an Eulerian grid resolution of  $N_x \times N_y$  greater than  $2049 \times 193$  also does not affect the computation results. Based on the results in Fig. 2, this study used  $\Delta s/L = 1/64$  and  $N_x \times N_y = 2049 \times 193$  to ensure the accuracy of the computation results.

### III. RESULTS AND DISCUSSION

The behavior of flexible filaments and fluid flow are scrutinized with the change of filament lengths ( $L$ ) and inclined angles ( $\theta$ ). Assuming the initial state of the filaments as unbent, the maximum length of the flexible filaments is determined depending on the inclined angle. In the adverse pressure gradient flow region, changes in the length and inclined angle of the flexible filaments can either form a backflow due to the adverse pressure gradient or block the backflow due to the filament's deflection. Figure 3 displays the examples of filament deflection and volume flow rate with variations in the filament length and the inclined angle. Figures 3(a)–3(aii) depict the case where the length of the filaments is insufficiently elongated compared to the inclined angle. In the transient flow regime, the flow is formed by the favorable pressure gradient, eventually reaching the steady flow regime. As the volume flow rate rapidly decreases in the adverse pressure gradient regime, the filaments deflect toward the direction of backflow. However, since the length of the filaments is not sufficient, the state allowing backflow remains continuous. Consequently, the volume flow rate will ultimately reach another steady flow regime with a converged negative value.

Figures 3(b)–3(bii) show the case where filaments of moderate length are provided for a given inclined angle. While the transient and steady flow regimes exhibit similar patterns, different phenomenon occurs in the adverse pressure gradient regime. The total volume flow rate, defined as the volume flow rate entering or exiting the channel at the inlet and outlet, and the volume flow rate across the filaments, defined as the flow through the space created between two filaments, are compared to investigate this phenomenon over time. As the filaments are sufficiently long, they deflect toward the backflow direction and eventually meet at a certain point. When the pathway between the two filaments vanishes, the volume flow rate across the filaments becomes zero. As a result, the two filaments act as a mechanical valve blocking the flow inside the channel. However, the total volume flow rate remains a small negative value, indicating that while there is no backflow between the filaments, the deflection of filaments in the backflow direction still generates backflow. In Figs. 3(b) and 3(bii), the two

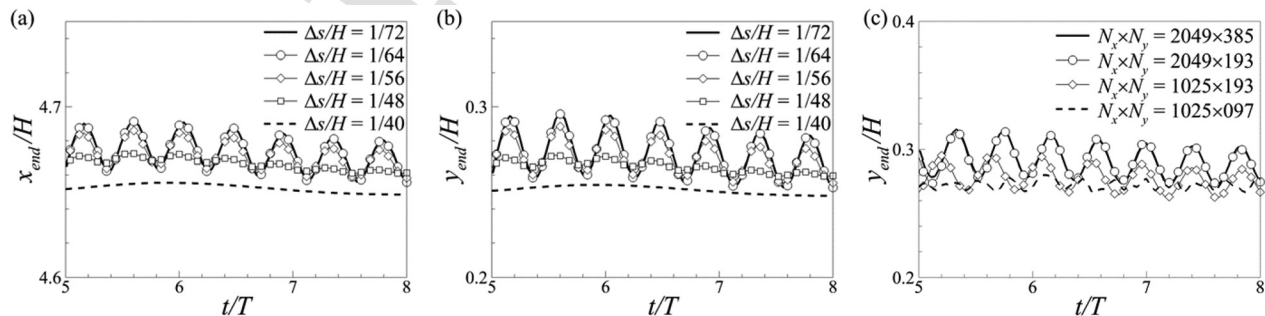
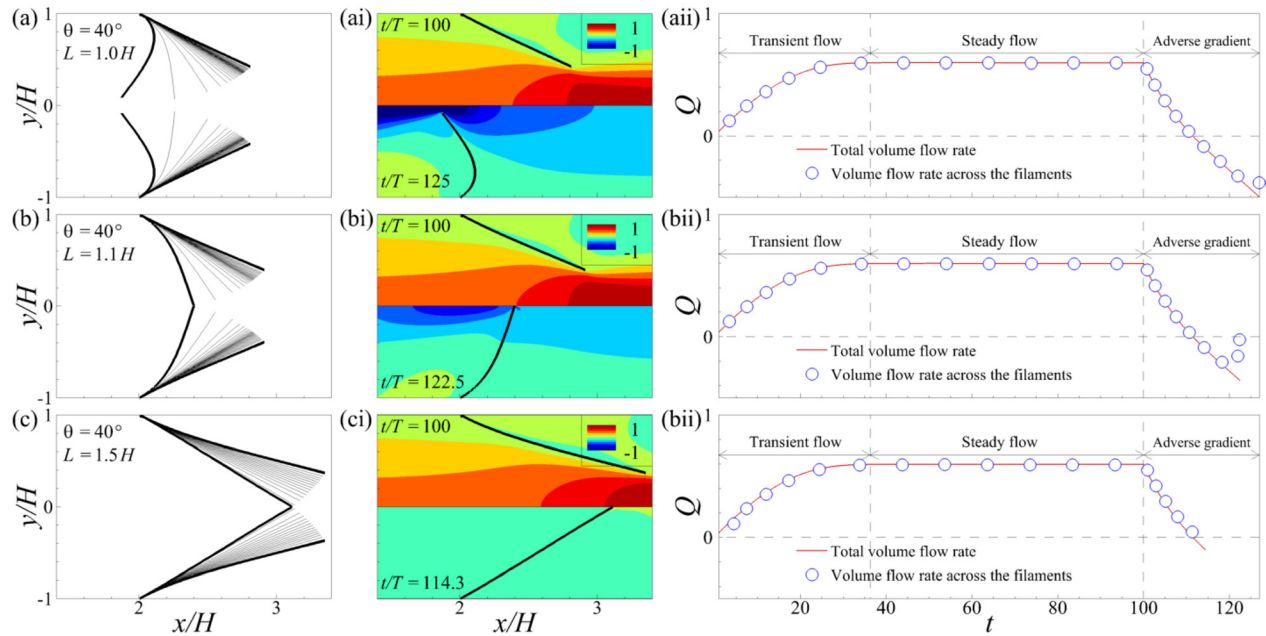


FIG. 2. The location of the end point of flexible filament at the (a) streamwise direction and (b) wall normal direction for various grid resolutions; (c) wall-normal direction for various mesh resolutions.



**FIG. 3.** Superposition of the flexible filaments from the initial and end states of adverse gradient flow for the cases of (a)  $\theta = 40^\circ$  and  $L = 1.0H$ ; (b)  $\theta = 40^\circ$  and  $L = 1.1H$ ; and (c)  $\theta = 40^\circ$  and  $L = 1.5H$ . The streamwise velocity ( $u$ ) around the filaments at the indicated time for the cases of (ai)  $\theta = 40^\circ$  and  $L = 1.0H$ ; (bi)  $\theta = 40^\circ$  and  $L = 1.1H$ ; and (ci)  $\theta = 40^\circ$  and  $L = 1.5H$ . Volume flow rate ( $Q$ ) depending on the time for the cases of (aii)  $\theta = 40^\circ$  and  $L = 1.0H$ ; (bii)  $\theta = 40^\circ$  and  $L = 1.1H$ ; and (cii)  $\theta = 40^\circ$  and  $L = 1.5H$ .

filaments act as a valve but cannot completely prevent backflow between them, as evidenced by the negative values of the volume flow rate across the filament in Fig. 3(bii). However, if the filaments' length is significantly long compared to the given inclined angle, the two filaments can completely block the backflow forming between them, acting as a mechanical valve. Figures 3(c)–3(cii) show the physical behavior in the case of very long filaments. In this case, the volume flow rate across the filaments gradually attenuates to zero, and the space between the two filaments disappears, acting as a mechanical valve. Nevertheless, the total volume flow rate remains a small negative value as the two filaments slightly deflect in the backflow direction, pushing the flow toward the inlet. Considering all these results, the flow can be categorized into three modes. Behavior of mode I is represented in Figs. 3(a)–3(aii). The length of the filaments is relatively short in mode I. It prevents the filaments to function as a mechanical valve within the channel flow. Consequently, the volume flow rate in the adverse pressure gradient regime monotonically decreases, acquiring a negative value under the influence of the adverse pressure gradient. It implies that the flow direction through the filaments is native in the streamwise direction. As a result, a flow opposite to that of the transient and steady flow regime is formed between the filaments, which can be defined as a backflow. Behavior of mode II is depicted in Figs. 3(b)–3(bii). The filament length in mode II is relatively longer than in mode I. Two filaments touch with each other at a certain time in the adverse pressure gradient regime, blocking the flow and acting as a mechanical valve within the channel flow. The volume flow rate continuously decreases to a negative value and then increases again, converging to zero. It suggests that the flow between the filaments momentarily adopts a negative in the streamwise direction but is

ultimately blocked. Therefore, a backflow is formed during part of the adverse pressure gradient regime, while the filament system works as a mechanical valve. A monotonic decrement of the volume flow rate to zero and contact of the filaments by deflection occur simultaneously within the adverse pressure gradient regime. As a result, the flow between the filaments always maintains a positive value in the streamwise direction before being ultimately blocked by the deflection of filaments. Hence, the filament system not only performs the role of the mechanical valve but also prevents backflow between the filament. Therefore, the present study classifies the flow modes based on the inclined angle and the filament length and analyzes the physical behavior of fluid for each corresponding mode. To this end, the start of the adverse pressure gradient regime  $t = 100T$  will be defined as  $T_{i,back}$ , and the time when the two filaments meet and start acting as a mechanical valve will be defined as  $T_{c,back}$ .

Figure 4(a) shows the variation in flow modes with changes in the inclined angle and the length of filaments. Here, the dashed line represents the longest length of filaments that do not interfere with each other without deflection, given the initial inclined angle condition. Thus, the two filaments will inevitably cause deflection due to a mutual interference outside the dashed line. In this case, the interaction between flexible bodies must be considered, and additional power is required to overcome the filament deflection to initiate the flow. Hence, this area was not considered in the present study. In most areas where  $L/H \approx 1.0$ , the filaments do not act as a mechanical valve and exhibit behavior similar to that in Fig. 3(a) (mode I). Therefore,  $T_{c,back}$  is not defined and does not appear in Fig. 4(b). The filaments act as a mechanical valve but allow backflow through them during adverse pressure gradient regime, exhibiting behavior similar to Fig. 3(b) in

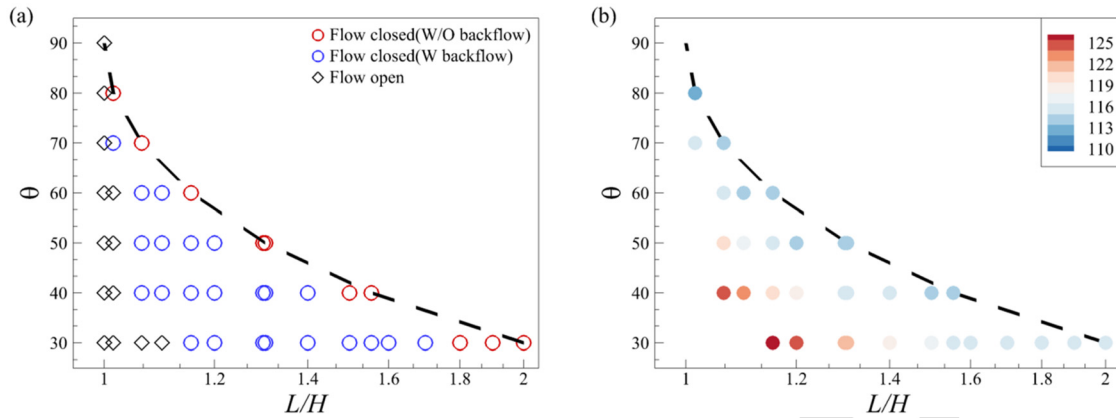


**FIG. 4.** Phase diagram of the flow closure due to the motion filaments within adverse gradient flow state, (b) closure times ( $T_{c,back}$ ) depending on the inclined angle ( $\theta$ ), and length of filaments ( $L$ ).

most other areas (mode II). Near the dashed line, the filaments display behavior akin to Fig. 3(c) (mode III). In other words, there is no backflow between the filaments during the adverse pressure gradient regime for filament configurations belonging to mode III. Since the filaments act as a mechanical valve in modes II and III,  $T_{c,back}$  is defined, but its value varies depending on the inclined angle and the filament length. Figure 4(b) illustrates the variation in  $T_{c,back}$  with changes in the inclined angle and filament length.  $T_{c,back}$  tends to decrease with a longer filament length and a larger inclined angle. As a result,  $T_{c,back}$  has a local minima at a specific  $\theta = 90^\circ$ ,  $L/H = 1/\sin 80^\circ \approx 1.02$ . However,  $T_{c,back}$  changes gradually due to the intersection between the filament length and the inclined angle near the dashed line, and it increases sharply as the filament configurations move away from the dashed line. The behavior of the filaments belongs to the one of three modes depending on the changes in the inclined angle and filament length, and the time  $T_{c,back}$ , when the filaments come into contact due to the adverse pressure gradient, varies. Subsequently, the study investigates the variation in the forces acting on the filaments during the adverse pressure gradient regime and the motion of the surrounding fluid flow.

It is necessary to arrange the forces acting on filaments into normal and tangential forces to the filament. The forces acting on the nodes of the filaments in the streamwise and wall-normal directions  $F_x$  and  $F_y$  can be obtained by using Eq. (9). The forces normal or tangential to filaments exerted on the filament can be evaluated by using  $F_x$ ,  $F_y$ , and the slope of filaments as shown in Eq. (15)

$$\begin{Bmatrix} F_T \\ F_N \end{Bmatrix} = \begin{bmatrix} \cos \theta_s & \sin \theta_s \\ -\sin \theta_s & \cos \theta_s \end{bmatrix} \begin{Bmatrix} F_x \\ F_y \end{Bmatrix}, \quad (15)$$

where  $\theta_s$  denotes the slope of the filaments at the nodes. Figures 5(a) and 5(b) show the normal and tangential forces acting on the filaments in the steady flow regime. In the steady flow regime, the predominant force on the filaments is the one maintaining their deflected state. As a result, the normal component of force  $f_N$  has a dominance influence in the steady flow regime. It is also observed that the change in the displacements of the filament's line elements leads to variations in  $f_N$  and  $f_T$ . As  $s$  moves from the clamped end ( $s/H = 0$ ) toward the free end

( $s = L$ ), the magnitude of  $f_N$  tends to decrease, while  $f_T$  increases. It indicates that  $f_N$  and  $f_T$  are forces resulting from different factors originated from the surrounding fluid flow. As the flow progresses from the steady flow regime to the adverse pressure gradient regime, the change in pressure gradient alters the flow direction. Consequently, the direction of the forces acting on the filaments changes within the adverse pressure gradient regime. Figures 5(ai) and 5(bi) display the normal and tangential forces acting on the filaments at the time when the direction of these forces changes. Here, the normal component of force  $f_N$  acting on the filaments converges to a value close to zero. It implies that the filaments are nearly in their initial state with minimal deflection and almost no force acting on them from the surrounding fluid flow. However, significant magnitudes of  $f_N$  and  $f_T$  are still present at the free end of the filaments. It indicates that the surrounding fluid flow still affect the free end of the filaments. Notably, the time depicted in Figures 5(ai) and 5(bi) changes with the length of the filament, and this change is inversely proportional to  $T_{c,back}$ . Therefore, it is necessary to maintain the direction of the forces acting on the filaments as close as possible to that in the steady flow regime to minimize  $T_{c,back}$ . Figures 5(aii) and 5(bii) illustrate the normal and tangential components of forces acting on the filaments at  $T_{c,back}$ . Here, the tangential component of force  $f_T$  shows a value close to zero. Consequently, the magnitude of the tangential force exhibits a monotonic decrease from the onset of the adverse pressure gradient regime similar to the case of the volume flow rate depicted in Fig. 3(cii). It suggests an existence of a positive correlation between the tangential force acting on the filament and changes in the velocity of the surrounding fluid flow. In contrast, the normal component of force  $f_N$  is relatively very large, especially as the  $L/H$  decreases. Since the free ends of filaments come into contact with each other to function as a valve at  $T_{c,back}$ , it is evident that the deflection of the filaments increases as the decrement of the filament length. Notably,  $f_N$  increases sharply near the free end filament elements, more so as  $L/H$  decreases. It implies the existence of the rapidly changing flow or pressure fields in the vicinity of the free end leading to a sharp increase in filament deflection. Additionally, it indicates that the stresses exerted by fluid flow on the filaments increase significantly as  $L/H$  decreases, suggesting that shorter  $L/H$  is not desirable for the stability or durability of the filaments. As a result, it was possible to



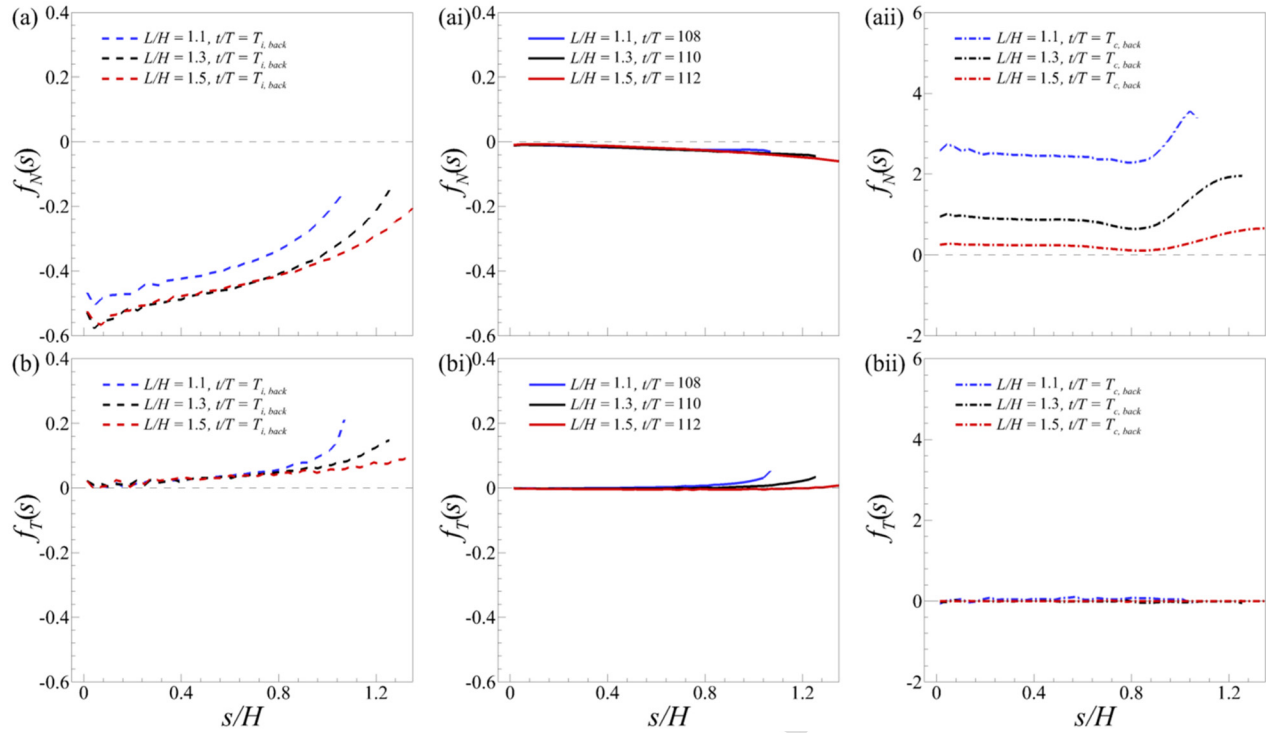


**FIG. 5.** Normal components of the force along the filament at (a)  $t/T = T_{i,back}$ , (ai) between  $T_{i,back}$  and  $T_{c,back}$ , and (aii)  $t/T = T_{c,back}$ , Tangential components of the force along the filaments at (b)  $t/T = T_{i,back}$ , (bi) between  $T_{i,back}$  and  $T_{c,back}$ , and (bii)  $t/T = T_{c,back}$ . Inclined angles  $\theta$  are  $40^\circ$  for all cases.

classify the forces acting on the filaments into normal and tangential directions through Fig. 5. It can be inferred that these two types of forces are generated due to two different factors on the fluid flow surrounding the filaments. Subsequently, the study aims to analyze the causes of the forces acting on the filaments by examining the vorticity fields and pressure fields around the filaments.

Figure 6 displays the distribution of the vorticity field around the filaments at the same time points as depicted in Fig. 5. Figures 6(a)–6(c) show the vorticity field distribution in the steady flow regime. The vortical structures detaching from the free end of the filaments are similar to the vortex rings observed in a cardiovascular flow (Zhang *et al.*, 2019; Zhang and Rival, 2020), and their mechanisms of formation can be

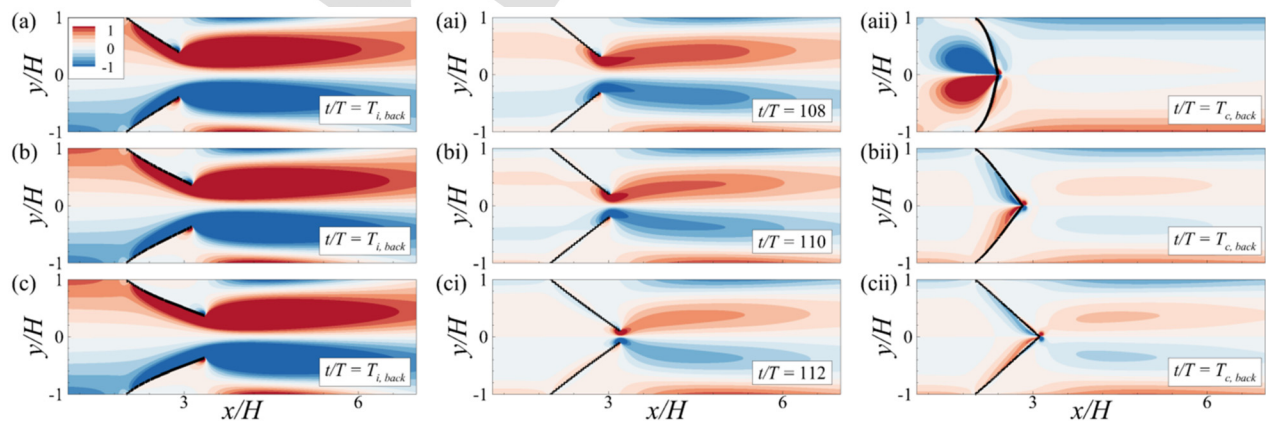


**FIG. 6.** Contour of  $\omega_z$  for the case with  $L = 1.1H$  at the (a)  $t/T = T_{i,back}$ , (ai) between  $T_{i,back}$  and  $T_{c,back}$ , and (aii)  $t/T = T_{c,back}$ ; For the case with  $L = 1.3H$  at the (b)  $t/T = T_{i,back}$ , (bi) between  $T_{i,back}$  and  $T_{c,back}$ , and (bii)  $t/T = T_{c,back}$ ; For the case with  $L = 1.5H$  at the (c)  $t/T = T_{i,back}$ , (ci) between  $T_{i,back}$  and  $T_{c,back}$ , and (cii)  $t/T = T_{c,back}$ . Inclined angles  $\theta$  are  $40^\circ$  for all cases.



considered analogous. The vortex ring formed at this time significantly influences the volume flow rate by developing a jet flow through the filaments (Querzoli *et al.*, 2010; Le and Sotiropoulos, 2013). Since the volume flow rate increases significantly around the filaments, the resultant vortex ring is well-developed, and the vortex ring is elongated along the streamwise direction. The intensity of the vortex ring has local maxima around the free end of the filaments. Moreover, as the vortex ring develops along the filaments, it can be associated with the behavior of filaments at all points. Figures 6(ai), 6(bi), and 6(cii) show the distribution of the vorticity field around the filaments at the same time points as Figs. 5(ai) and 5(bi). Due to the adverse pressure gradient, the flow rate is significantly weakened, resulting in a much weaker intensity and development of the vortex ring compared to Figs. 6(a)–6(c). Additionally, since the vortical structure forms only near the free end of the filaments, the interaction between the vortical structure and the filaments is limited to the vicinity of the free end of filaments. Furthermore, it can be observed that as the length of the filaments increases, the intensity of the vortex ring formed near the free end weakens. This implies that at the time points of Figs. 6(ai), 6(bi), and 6(cii), the interaction between the filaments and the vortical structures diminishes as the length of the filaments increases. Figures 6(aii), 6(bii), and 6(cii) illustrate the distribution of vorticity field around the filaments at  $T_{c,back}$ . In Fig. 6(aii), since  $T_{c,back}$  is relatively large, it can be inferred that the vortex ring has significantly weakened or even disappeared. Additionally, the formation of vortical structures induced by a relatively strong backflow is observed in the front part of the filaments. In Figs. 6(bii) and 6(cii), while a vortex ring is still present behind the filaments, its size is greatly diminished. The vortex rings formed at  $T_{c,back}$  are more a result of the circulation of the fluid flow along the filaments rather than the volume flow rate passing through the filaments. The vortex ring is not attached to the filaments but are positioned relatively far from them, and their intensity remains much weaker compared to the cases of Fig. 6(aii), 6(bii), and 6(cii). It indicates that the interaction between the filaments and the vortical structures is either non-existent or significantly reduced at the result of Fig. 6(aii), 6(bii), and 6(cii). In summary, based on the results presented in Fig. 6, the following can be concluded: (i) During the adverse pressure gradient regime, the magnitude of interaction

between the filaments and vortical structures decreases monotonically. (ii) The interaction between the filaments and vortical structures mainly occurs near the free end of the filaments with relatively weaker interactions near the clamped end. This aligns well with the trends of  $f_T$  observed in Fig. 5. Notably, the direction of the tensile force exerted on the filaments in Figs. 5(b) and 5(bi) coincides with the direction of the vortical structures seen in Fig. 6. It suggests that the tangential force on the filaments is primarily a viscous force generated by the vortical structures. While the vortical structures shown in the vorticity fields explain the  $f_T$  acting on the filaments well, the behavior of the vortical structure does not sufficiently account for normal components of force exerted on the filaments. Therefore, subsequent analysis will focus on investigating the forces acting on the filaments through the pressure fields around the filaments.

Figure 7 displays the pressure field distribution at the same time and locations as in Figs. 5 and 6. Figures 7(a)–7(c) show the distribution of pressure field around the filaments within the steady flow regime. A monotonic decrease in the pressure field is observed along the streamwise direction due to the favorable pressure gradient. The pressure difference around the filaments is greatest near the clamped end and smallest near the free end, implying that the force exerted on the filaments by the pressure is largest near the clamped end and smallest near the free end. Figures 7(ai), 7(bi), and 7(cii) correspond to the same time as Figs. 5(ai), 5(bi), 6(ai), 6(bi), and 6(cii), showing the pressure field distribution. The difference in the pressure field magnitude across the filaments is maintained at a very weak level. It indicates that the force generated by the pressure difference around the filaments is relatively small. For the case of relatively short filament lengths [ $L = 1.1H$  in Fig. 7(ai)], the absence of a significant pressure field difference around the filaments suggests that the force due to pressure difference is almost negligible. It can be inferred that as filament length decreases, the magnitude of the force exerted on the filaments by pressure during the adverse pressure gradient regime is likely to decrease. Figures 7(aii), 7(bii), and 7(cii) illustrate the distribution of the pressure field around the filaments at  $T_{c,back}$ . The pressure distribution at  $T_{c,back}$  shows a monotonic increase along the streamwise direction due to the influence of the adverse pressure gradient and the

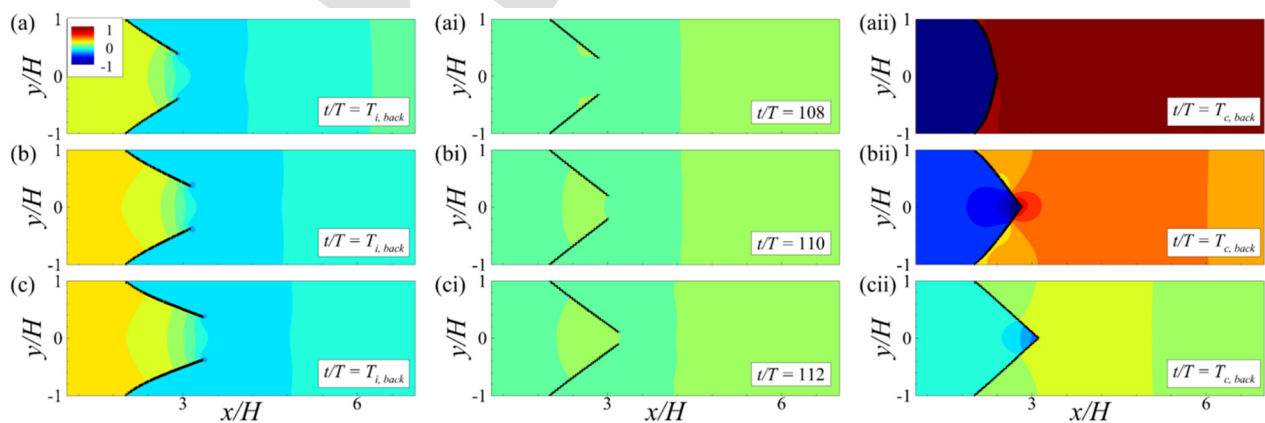


**FIG. 7.** Contour of pressure for the case with  $L = 1.1H$  at the (a)  $t/T = T_{i,back}$ , (ai) between  $T_{i,back}$  and  $T_{c,back}$ , and (aai)  $t/T = T_{c,back}$ ; For the case with  $L = 1.3H$  at the (b)  $t/T = T_{i,back}$ , (bi) between  $T_{i,back}$  and  $T_{c,back}$ , and (bii)  $t/T = T_{c,back}$ ; For the case with  $L = 1.5H$  at the (c)  $t/T = T_{i,back}$ , (ci) between  $T_{i,back}$  and  $T_{c,back}$ , and (cii)  $t/T = T_{c,back}$ . Inclined angles  $\theta$  are  $40^\circ$  for all cases.

filaments acting as a mechanical valve. Similar to Figs. 7(ai), 7(bi), and 7(cii), the pressure difference around the filaments at  $T_{c,back}$  increases as the filament length decreases. Notably, the pressure difference increases significantly near the free end rather than the clamped end, likely due to the pressure being transmitted along the circulation of the flow around the filaments shown in Fig. 6. In summary, based on the results from Fig. 7: (i) In the steady flow regime, the interaction between the pressure field and the filaments strengthens as the filament length increases, especially reaching maximum values near the clamped end. (ii) In the adverse pressure gradient regime, this interaction weakens as the filament length increases, with the minimum values occurring near the clamped end. These results show the good agreements with the trend of  $f_N$  shown in Fig. 5. Particularly, the regions of sharp increase in pressure difference in Figs. 7(aii), 7(bii), and 7(cii) coincide with the regions of rapid increase in  $f_N$  in Fig. 5(aii). It suggests that the normal force acting on the filaments is a pressure force formed due to the pressure difference across the filaments.

The variation in the forces acting on the filaments due to changes in the filament length can be explained using the vorticity and pressure fields. However, the behavior of the filaments during the adverse pressure gradient regime and  $T_{c,back}$  are influenced not only by the filament length but also by the inclined angle. Figure 8 illustrates the variation in the forces acting on the filaments classified into normal and tangential components with changes of the inclined angle. Figures 8(a) and 8(b) show the normal and tangential component forces acting on the filament elements in the steady flow regime. It indicates that an

increment of the inclined angle enhances the forces exerted on the filaments. The variation in normal and tangential components of forces due to changes in the inclined angle is more significant than that in the filament length, as seen in Fig. 5. It suggests that the mechanical valve system composed of two filaments is more sensitive to changes in the inclined angle than the length of filament. Figures 8(ai) and 8(bi) show the variation in forces acting on the filaments at the time when the direction of the forces is altered. The forces exerted on the filaments are almost negligible excluding the free end of filaments, similar to the result of Figs. 5(ai) and 5(bi). It implies that the filaments are in a state similar to their non-deflected initial condition. Additionally,  $t/T$  at Figs. 8(aii) and 8(bi) varies with changes of the inclined angle, and this variation is inversely proportional to  $T_{c,back}$ . It implies that an increment of the inclined angle has a similar influence on an increment of the filament length. Figures 8(aii) and 8(bii) classify the components of forces exerted on the filaments at  $T_{c,back}$  into normal and tangential components. The forces vary with the displacements of the line elements similar to the result of Figs. 5(aii) and 5(bii), but the increment in  $f_N$  around the free end of filaments is more abrupt. It reveals that the valve system composed of filaments is more sensitive to changes in the inclined angle than to the filament length, and that decreasing the inclined angle to reduce the filament load in the steady flow regime may significantly increase the filament load in the adverse pressure gradient regime.

The variations of the normal and tangential components of forces exerted on filaments can be analyzed by using vorticity and pressure fields for the changes of the inclined angle, as shown in Figs. 6 and 7.

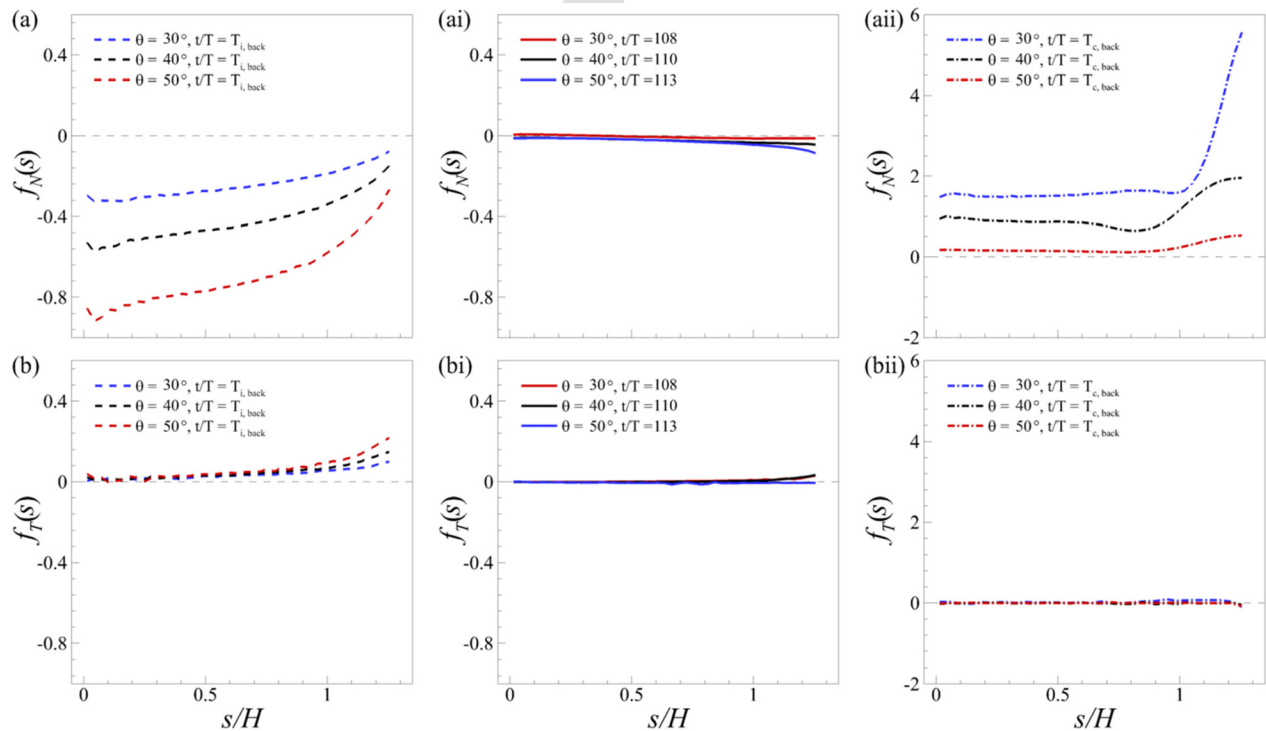


**FIG. 8.** Normal components of the force along the filament at (a)  $t/T = T_{i,back}$ , (ai) between  $T_{i,back}$  and  $T_{c,back}$ , and (aii)  $t/T = T_{c,back}$ . Tangential components of the force along the filaments at (b)  $t/T = T_{i,back}$ , (bi) between  $T_{i,back}$  and  $T_{c,back}$ , and (bii)  $t/T = T_{c,back}$ . Length of filaments  $L$  are  $1.3H$  for all cases.

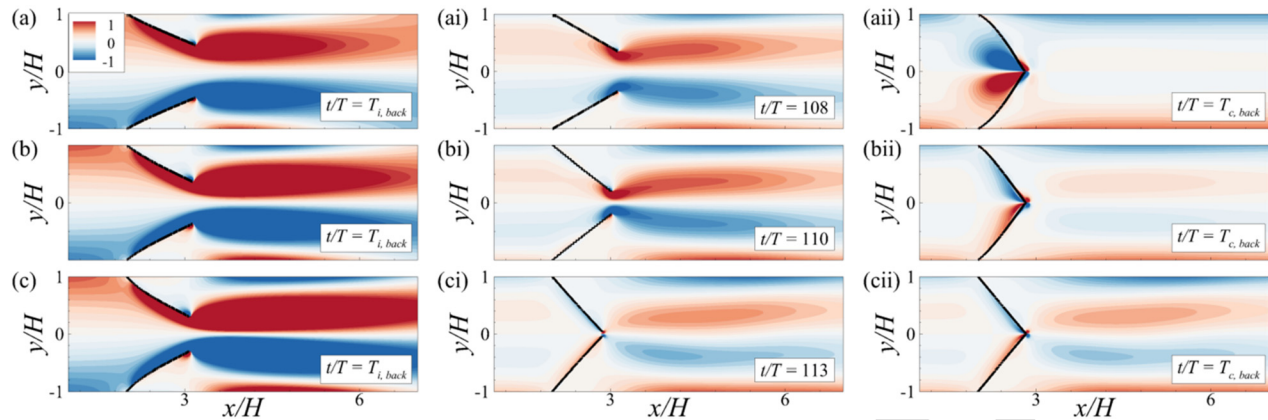


**FIG. 9.** Contour of  $\omega_z$  for the case with  $\theta = 30^\circ$  at the (a)  $t/T = T_{i,back}$ , (ai) between  $T_{i,back}$  and  $T_{c,back}$ , and (aii)  $t/T = T_{c,back}$ ; For the case with  $\theta = 40^\circ$  at the (b)  $t/T = T_{i,back}$ , (bi) between  $T_{i,back}$  and  $T_{c,back}$ , and (bii)  $t/T = T_{c,back}$ ; For the case with  $\theta = 50^\circ$  at the (c)  $t/T = T_{i,back}$ , (ci) between  $T_{i,back}$  and  $T_{c,back}$ , and (cii)  $t/T = T_{c,back}$ . Length of filaments  $L$  are  $1.3H$  for all cases.

Figure 9 represents the vorticity field around filaments at the same instance as Fig. 8. Figures 9(a)–9(c) reveal the vorticity field in the steady flow regime. Figures 9(a)–9(c) clearly illustrate the vortex ring, similar for the case of the length of filaments shown in Figs. 6(a)–6(c). The intensity of the vortex ring is amplified with an increment of the inclined angle, especially near the free end of the filaments. The trend of the tangential force  $f_T$  shows similar trends with a result in Fig. 8(b), matching the vorticity field around the filaments. Since  $f_T$  is very small in Fig. 8(bi), the corresponding vortex ring should be weakened compared to the results in Figs. 9(a)–9(c). Figures 9(ai), 9(bi), and 9(cii) substantiate it. Vortex ring with a weak level only resides in the vicinity of the free end of filaments. The intensity of the vortex ring diminishes with increasing inclined angle. It is also coincide with weak  $f_T$  near the free end of the filaments in Fig. 8(bi). The intensity of vortex ring is either greatly weakened or diminished, or detached from the free end of the filaments at  $T_{c,back}$ , as shown in Figs. 9(aii), 9(bii), and 9(cii). It is also coincide with the near-zero magnitude of  $f_T$  in Fig. 8(cii). The remaining weakened vortex ring appears to be formed not by the

volume flow rate, as in Fig. 6, but by flow circulation along the filaments. Additionally, a vortical structure in Fig. 9(aii) is formed at the front of the filaments similar to Fig. 6(aii). Likewise, the front vortical structure in Fig. 9(aii) is formed by the backflow during the adverse pressure gradient regime due to the large  $T_{c,back}$ .

In Fig. 8, the normal force  $f_N$  on filaments can be examined by using the distribution of the pressure field around the filaments. Similar approaches can be employed to investigate the distribution of the pressure field in Fig. 10. The distribution of pressure fields in the steady flow regime can be seen in Figs. 10(a)–10(c), where the pressure distribution shows a monotonic decrease along the streamwise direction. Additionally, the pressure difference formed across the filaments increases with the increment of the inclined angle. Trends of the pressure difference resembles with the variation of  $f_N$  in Fig. 8(a), similar to the results of Figs. 7(a)–7(c). The pressure difference shows the abrupt increment around the clamped end and decrement in the vicinity of the free end of the filaments. It indicates that the  $f_N$  primarily arises from the pressure difference acting on the filaments within the

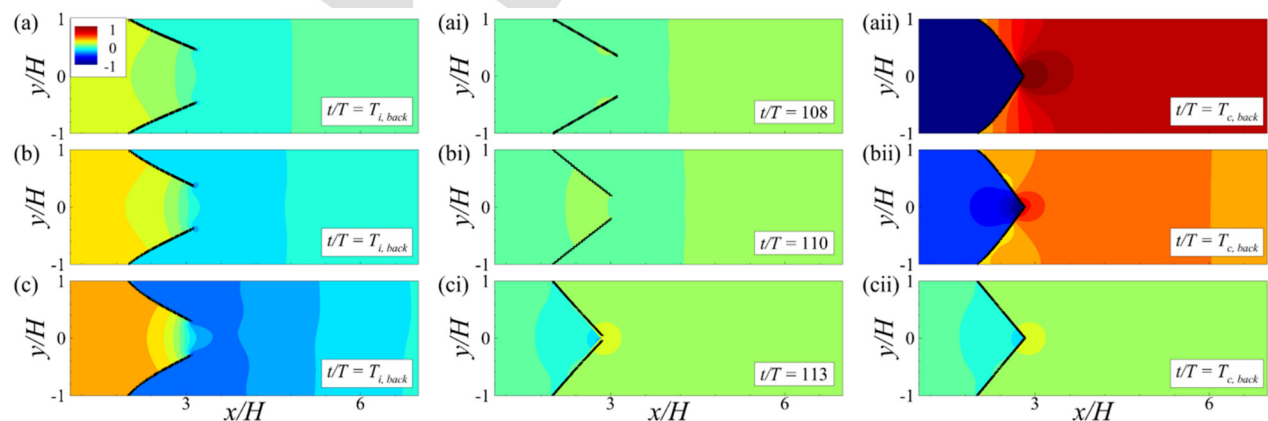


**FIG. 10.** Contour of pressure for the case with  $\theta = 30^\circ$  at the (a)  $t/T = T_{i,back}$ , (ai) between  $T_{i,back}$  and  $T_{c,back}$ , and (aii)  $t/T = T_{c,back}$ ; For the case with  $\theta = 40^\circ$  at the (b)  $t/T = T_{i,back}$ , (bi) between  $T_{i,back}$  and  $T_{c,back}$ , and (bii)  $t/T = T_{c,back}$ ; For the case with  $\theta = 50^\circ$  at the (c)  $t/T = T_{i,back}$ , (ci) between  $T_{i,back}$  and  $T_{c,back}$ , and (cii)  $t/T = T_{c,back}$ . Length of filaments  $L$  are  $1.3H$  for all cases.



steady flow regime. Figures 10(ai), 10(bi), and 10(ci) represent the pressure field at the same instance as Figs. 8(ai), 8(bi), 9(ai), 9(bi), and 9(ci). Since the magnitude of  $f_N$  in Fig. 8(ai) is nearly zero, the pressure difference across the filaments in Figs. 10(ai), 10(bi), and 10(ci) is maintained at a low level. In cases of a relatively large inclined angle ( $\theta = 50^\circ$ ), the pressure difference around the filaments is significant. It coincides with the increment of  $f_N$  in Fig. 8(ai) for the same inclined angle. The pressure fields at  $T_{c,back}$  are illustrated in Figs. 10(aii), 10(bii), and 10(cii). The pressure difference across the filaments increases sharply with the decrement of the inclined angle, similar to the case when the length of filament decreases. Additionally, the pressure difference across the filaments increases from the clamped end to the free end, consistent with the trend of  $f_N$  in Fig. 8(aii). In summary, the forces exerted on the filaments due to changes of the inclined angle are mainly affected by  $f_N$  from the surrounding pressure fields and  $f_T$  from the vorticity fields. Both the inclined angle and the filament length, which determine the geometrical shape of the filament valve system, are primary variables affecting the forces exerted on the filaments through pressure and vorticity fields considering the results from Figs. 5–7. Based on these results, we will propose indicators for evaluating the efficiency of the filament system using mechanical factors such as volume flow rate through the filament system,  $T_{c,back}$ , and power consumption. It will lead to presenting an optimized configuration of the filament valve system based on the inclined angle and length of the filaments.

As shown in Fig. 4, the behavior of filaments depending on their configuration can be classified into three modes. Filaments should be acted as a mechanical valve for modes II and III. For the case of filaments belong to modes II and III, the efficiency of a mechanical valve can be defined. Various approaches had been proposed to define the efficiency of a mechanical valve. Pierrakos and Vlachos (2006) proposed hydrodynamic efficiency for biological leaflet valves. The definition of hydrodynamic efficiency is given in Eq. (16)

$$\eta_v = \frac{\text{Useful Work}}{\text{Useful Work} + \text{Wasted Energy}}. \quad (16)$$

In the present study, useful work is defined as the kinetic energy of the flow passing through the valve, while wasted energy encompasses the energy expended in viscous dissipation, frictional drag at the channel wall, and the work done to deflect the filaments. The sum of useful work and wasted energy equals the total work used to operate the mechanical valve including both the filaments and the channel. The magnitude of total work can be evaluated by using the 1st law of thermodynamics, as expressed in Eq. (17)

$$\dot{W}_{valve} = \dot{m}_{fluid} \left( \frac{\bar{p}_{outlet} - \bar{p}_{inlet}}{\rho_{fluid}} + \frac{\bar{u}_{outlet}^2 - \bar{u}_{inlet}^2}{2} \right), \quad (17)$$

where  $\bar{\phantom{x}}$  indicates the time-averaged properties. According to the principle of mass conservation, the flow rate passing through the inlet and outlet of the channel is identical, leading to the relationship  $u_{outlet} = u_{inlet}$ . Consequently, the hydrodynamic efficiency can be simplified and expressed as shown in Eq. (18)

$$\eta_v = \frac{\dot{m}_{fluid} \cdot \bar{u}_{valve}^2}{2\dot{W}_{valve}}. \quad (18)$$

The hydrodynamic efficiency defined in Eq. (18) can be interpreted as the ratio between the kinetic energy of the flow passing through the valve and the power consumption required to pass the flow through the filament valve. The hydrodynamic efficiency during the steady flow regime should be employed by using Eq. (18). On the other hand, the adverse pressure gradient during the adverse pressure gradient regime is formed due to unintended external perturbation rather than as a part of desirable work. Consequently, the hydrodynamic efficiency during the adverse pressure gradient regime can be defined as the ratio between the power consumption during the steady flow regime and the average kinetic energy of the flow during the adverse pressure gradient regime. It can be simplified and defined as Eq. (19)

$$\eta_{v,back} = \frac{0.5 \cdot \dot{m}_{fluid,back} \cdot u_{valve,back}^2}{\dot{W}_{valve,steady}}. \quad (19)$$

Figure 11(a) demonstrates the magnitude of power consumption by the filament valve and channel within the steady flow regime. It reveals that as the inclined angle of the filament increases, the power consumption of the mechanical filament valve also increases. Furthermore, an increment of the length of the filaments increases the power consumption for a constant inclined angle. It indicates that the most critical geometric variable determining the performance of the mechanical valve is the inclined angle for the perspective of energy consumption. The increase in power consumption with the inclined angle is due to various factors. Figure 9 shows that as the inclined angle increases, the vortex ring formed by the filaments becomes more pronounced. This implies that part of the power consumption is used to develop the vortical structure with increasing inclined angle. Also, a larger inclined angle forms the larger deflection of filament to reach the steady flow regime, as evidenced by the increase in  $f_N$  in the steady flow regime shown in Fig. 8. Therefore, part of the power consumption is also used to maintain the elastic energy due to deflection of the filaments. An increase in the length of filaments shows a similar trend to the increase in the inclined angle, as seen in Figs. 5 and 6. However, the flow parameter changes more sensitively with an increment of the inclined angle than of the filament length. It leads to a more sensitive response in power consumption to changes in the inclined angle. Consequently, the hydrodynamic efficiency in the steady flow regime is more sensitive to changes of the inclined angle than changes of filaments length. Figure 11(b) displays the hydrodynamic efficiency during the steady flow regime. Hydrodynamic efficiency appears to be inversely proportional to power consumption. It suggests that most of the variation in power consumption shown in Fig. 11(a) does not contribute to the kinetic energy of the flow. Therefore, maintaining a smaller inclined angle in a filament valve system is advantageous from an efficiency perspective without considering backflow issues. Figure 11(c) displays the hydrodynamic efficiency of the filament valve during the adverse pressure gradient regime. The results in Fig. 11(c) indicate that the hydrodynamic efficiency is more influenced by the filament length than by the inclined angle within the adverse pressure gradient regime. The hydrodynamic efficiency is maintained at a very low level in the region where both the inclined angle and the filament length are small, which belongs to mode II and is close to mode I in Fig. 4. It is due to the high level of backflow caused by a relatively large  $T_{c,back}$  in this region. Conversely, the region with very large inclined angles also



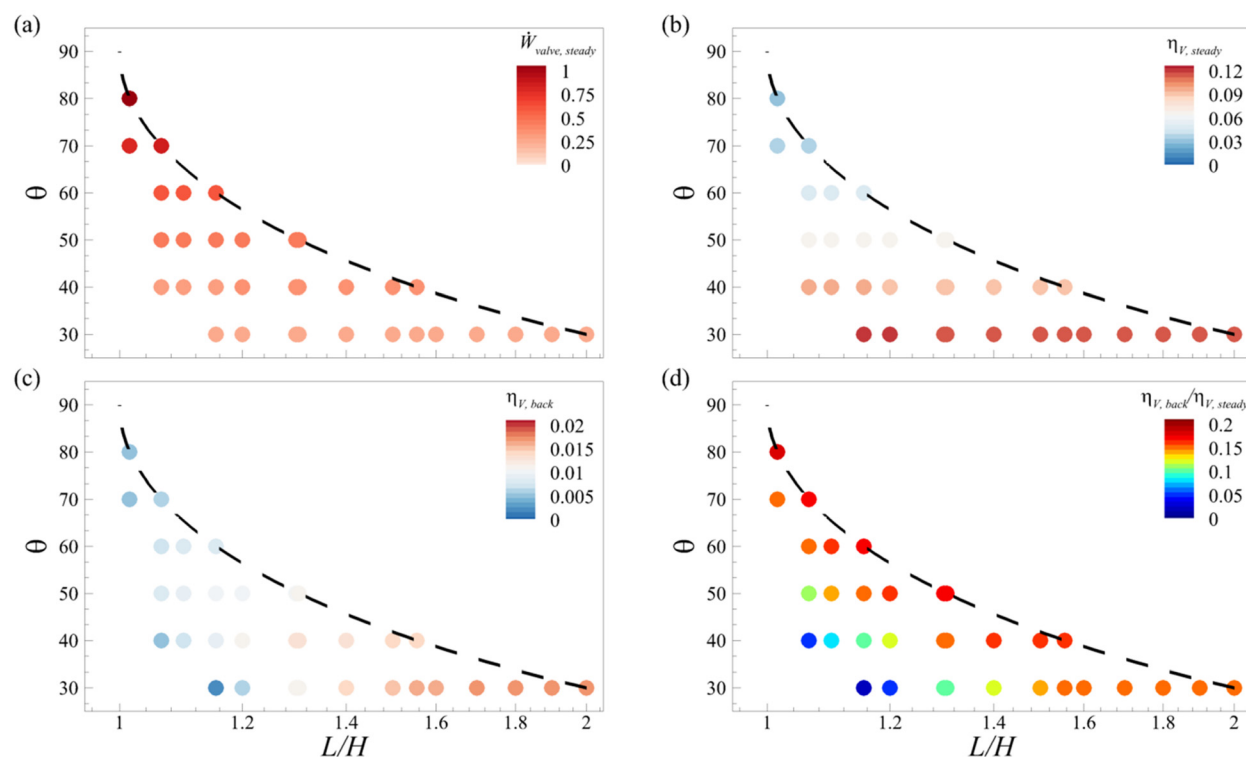


**FIG. 11.** (a) Average power consumption during the steady flow regime ( $\dot{W}_{valve, steady}$ ), (b) Average hydrodynamic efficiency during the steady flow regime ( $\eta_{V, steady}$ ), (c) Average hydrodynamic efficiency during the adverse pressure gradient regime ( $\eta_{V, back}$ ), and (d)  $\eta_{V, back}/\eta_{V, steady}$  depending on the length of filaments ( $L$ ) and inclined angle ( $\theta$ ).

shows relatively low hydrodynamic efficiency because of the high power consumption required by the filament valve in this region. Additionally, the performance of the filament valve can be evaluated based on how much of the kinetic energy formed during the steady flow regime is maintained during the adverse pressure gradient regime. Figure 11(d) shows the ratio of kinetic energy between the steady flow regime and the adverse pressure gradient regime. The ratio between kinetic energies is inversely proportional to the  $T_{c, back}$  pattern shown in Fig. 4(b). Consequently, Fig. 11 implies the following: For flow systems that frequently experience backflow or are very sensitive to backflow, it is necessary to minimize backflow caused by unintended adverse pressure gradients. Such flow systems might reasonably choose filament valves with a high inclined angle and the corresponding filament length, even if this results in higher power consumption. On the other hand, for flow systems that are less sensitive to backflow, it would be rational to choose filament valves with a low inclined angle and a very long filament length, characteristics that generally result in lower power consumption.

The performance of a filament valve is influenced not only by its geometric structure but also by the properties of the filament material. Figure 12 shows the changes in the performance of the filament valve with variations in one of the key material properties: bending rigidity. An increase in bending rigidity implies an increment of the flow resistance of the filaments against the flow. Therefore, it is reasonable to expect that the power consumption of the filament valve increases

with an increment of bending rigidity. The relationship between bending rigidity and the power consumption of the filament valve is depicted in Fig. 12(a). Hydrodynamic efficiency in the steady flow regime should exhibit a decreasing trend with an increment of bending rigidity because of the higher power consumption due to the increment of flow resistance. The tendency in hydrodynamic efficiency is presented in Fig. 12(b). As the influence of increased power consumption due to bending rigidity is predominant, the hydrodynamic efficiency in the adverse pressure gradient regime also tends to decrease monotonically, which can be verified in Fig. 12(c). Since hydrodynamic efficiency is predominantly affected by power consumption, the ratio of hydrodynamic efficiency between the steady flow regime and the adverse pressure gradient regime can be used to assess the volume flow rate or the kinetic energy of the flow. Figure 12(d) shows the ratio of hydrodynamic efficiency between these two regimes. The rate of deflection change in the filaments due to the adverse pressure gradient is attenuated with an increment of bending rigidity, resulting in an increment of  $T_{c, back}$  and a decrement of the accumulated volume flow rate passing through the filaments due to backflow. These results are consistent with the works of Calandrini and Aulisa (2019), which revealed that an increase in Young's modulus leads to a decrease in the accumulated volume flow rate through the valve. Therefore, in most ranges of bending rigidity, the ratio of hydrodynamic efficiency tends to decrease with an increase in bending rigidity. Conversely, when bending rigidity is very low, the

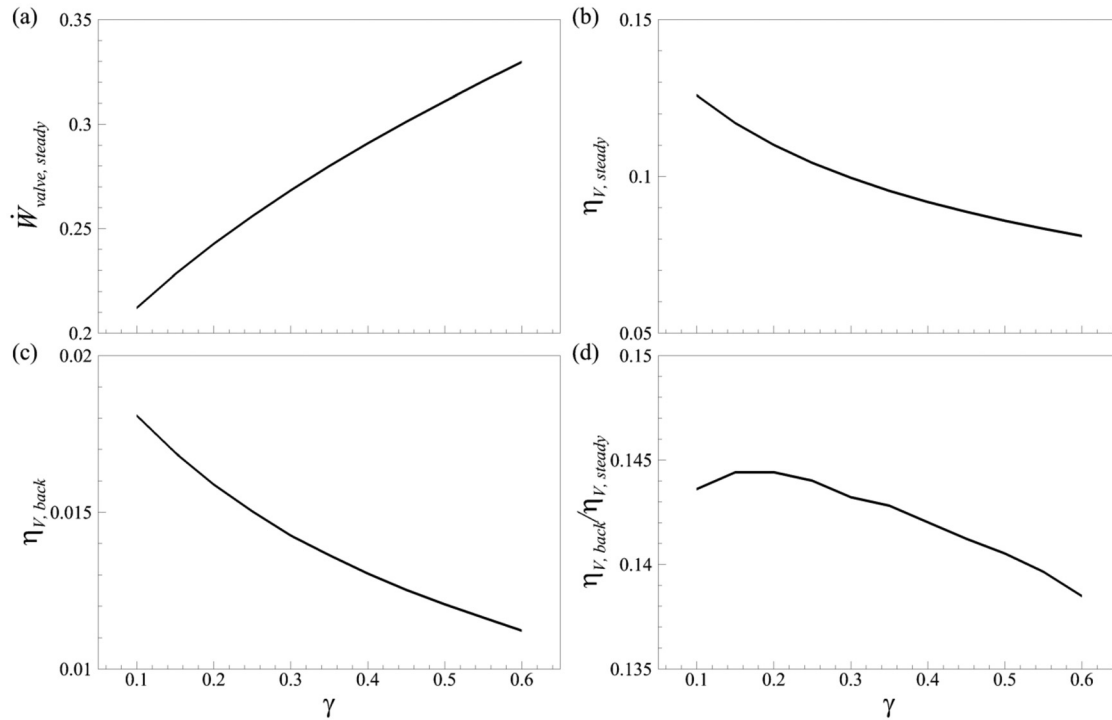


**FIG. 12.** (a) Average power consumption during the steady flow regime ( $\dot{W}_{\text{valve,steady}}$ ), (b) average hydrodynamic efficiency during the steady flow regime ( $\eta_{V,\text{steady}}$ ), (c) average hydrodynamic efficiency during the adverse pressure gradient regime ( $\eta_{V,\text{back}}$ ), and (d)  $\eta_{V,\text{back}}/\eta_{V,\text{steady}}$  depending on the bending rigidity.

magnitude of backflow reduces, but the accumulated volume flow rate decreases or converges due to the small  $T_{c,\text{back}}$ . Hence, in cases of very low bending rigidity, the ratio of hydrodynamic efficiency decreases as bending rigidity decreases.

#### IV. SUMMARY AND CONCLUSIONS

The behavior of a mechanical filament valve, mimicking a biological leaflet valve, is analyzed using the immersed boundary method. As a favorable pressure gradient is applied in the channel, the two filaments clamped on the channel wall allow the flow to pass through the channel. However, the two filaments prevent the flow within the channel when the adverse pressure gradient is applied in the channel. These behaviors of the filaments vary depending on the length of filaments ( $L$ ) and the initial inclined angle of filaments ( $\theta$ ). It can also be classified into three modes based on the difference in volume flow rates passing through the filaments: Mode I, where filaments fail to act as a mechanical valve and allow the backflow through the channel; mode II, where filaments act as a mechanical valve and allow the backflow in some section; and mode III, where filaments act as a mechanical valve and prevent the backflow. For the case of modes II and III, the time when the flow within the channel is blocked by the filaments can be defined as  $T_{c,\text{back}}$ .  $T_{c,\text{back}}$  varies with changes in  $L$  and  $\theta$ , and maximum values of  $T_{c,\text{back}}$  is 2.5 times larger than its minimum values. This variation of  $T_{c,\text{back}}$  occurs due to the changes in the magnitude and direction of forces acting on the filaments. The forces acting on the filaments are scrutinized using the forces in tangential ( $f_T$ ) and normal ( $f_N$ ) directions, and  $f_N$  has a dominant influence on the deflection

of filaments.  $f_N$  tends to decrease gradually with increasing  $L$  and shows a similar trend with increasing  $\theta$  at  $T_{c,\text{back}}$ . Vorticity fields in the vicinity of filaments show that the forces in the tangential direction ( $f_T$ ) are organized with the vortical structures formed by the behavior of filaments, known as the vortex ring. On the other hands, pressure fields around the filaments insist that the forces in the normal direction ( $f_N$ ) are associated with the distribution of pressure fields around the filaments. The filaments not only act as a valve against the flow created by the adverse pressure gradient but also serve as a flow resistance against flow created by the favorable pressure gradient. Hydrodynamic efficiency ( $\eta_{V,\text{steady}}$ ) of the filaments against the flow by favorable gradient is defined, and the changes in  $\eta_{V,\text{steady}}$  with variations in  $L$  and  $\theta$  are observed. The local maximum hydrodynamic efficiency occurs at  $(L, \theta) = (1/\sin 60^\circ, 30^\circ)$ , and the local minimum at  $(L, \theta) = (1/\sin 80^\circ, 80^\circ)$ , with a difference of about 5.0 times. The ratio of kinetic energy in the flow during the adverse pressure gradient regime and steady flow regime ( $\eta_{V,\text{back}}/\eta_{V,\text{steady}}$ ) is employed to analyze the efficiency of filaments as a mechanical valve. The maximum value of  $\eta_{V,\text{back}}/\eta_{V,\text{steady}}$  is observed at  $(L, \theta) = (1/\sin 80^\circ, 80^\circ)$ , and the minimum value of ( $\eta_{V,\text{back}}/\eta_{V,\text{steady}}$ ) occurs at  $(L, \theta) = (1/\sin 60^\circ, 30^\circ)$ . It shows the opposite trends to the change of  $\eta_{V,\text{steady}}$  and  $T_{c,\text{back}}$ . It implies that reducing the flow resistance of the filament valve and the time sensitivity of the valve response is not possible simultaneously. The changes of  $\eta_{V,\text{steady}}$  and  $\eta_{V,\text{back}}/\eta_{V,\text{steady}}$  are scrutinized with the variation in the bending rigidity ( $\gamma$ ) of the filaments.  $\eta_{V,\text{steady}}$  shows a monotonic change with a change of bending rigidity, but  $\eta_{V,\text{back}}/\eta_{V,\text{steady}}$  reaches its maximum value in the vicinity of  $\gamma = 0.2$ .

## 812 ACKNOWLEDGMENTS

813 This work was supported by the National Research Foundation of  
814 Korea (NRF) grant funded by the Korea Government (MSIT) (Grant  
815 No. RS-2023-00274580) and “Regional Innovation Strategy (RIS)”  
816 through the National Research Foundation of Korea (NRF) funded by  
817 the Ministry of Education (MOE) (Grant No. 2023RIS-009).

## 819 AUTHOR DECLARATIONS

## 820 Conflict of Interest

821 The authors have no conflicts to disclose.

## 822 Author Contributions

823 **Jongmin Yang:** Conceptualization (lead); Data curation (lead); Formal  
824 analysis (lead); Funding acquisition (lead); Investigation (lead);  
825 Methodology (lead); Project administration (lead); Resources (lead);  
826 Software (lead); Supervision (lead); Validation (lead); Visualization  
827 (lead); Writing – original draft (lead); Writing – review & editing (lead).

## 829 DATA AVAILABILITY

830 The data that support the findings of this study are available from  
831 the corresponding author upon reasonable request.

## 832 REFERENCES

- 833 Asghar, Z., Khan, M. W. S., Gondal, M. A., and Ghaffari, A.,  
834 “Magnetohydrodynamic flow of Carreau Yasuda fluid inside a complex wavy  
835 passage formed by beating cilia: A finite-difference analysis,” *Proc. Inst. Mech.*  
836 *Eng.*, Part E (published online 2023a).
- 837 Asghar, Z., Khan, M. W. S., Pasha, A. A., Rahman, M. M., Sankaralingam, L., and  
838 Alam, M. I., “On non-Newtonian fluid flow generated via complex metachronal  
839 waves of cilia with magnetic, hall, and porous effects,” *Phys. Fluids* **35**, 093601  
840 (2023b).
- 841 Borazjani, I., “Fluid-structure interaction, immersed boundary-finite element  
842 method simulations of bio-prosthetic heart valves,” *Comput. Methods Appl.*  
843 *Mech. Eng.* **257**, 103–116 (2013).
- 844 Calandrini, S. and Aulisa, E., “Fluid-structure interaction simulations of venous  
845 valve: A monolithic ALE method for large structural displacements,” *Int. J.*  
846 *Numer. Methods Biomed. Eng.* **35**(2), ■ (2019).
- 847 Choi, Y. J., Vedula, V., and Mittal, R., “Computational study of the dynamics of a  
848 bileaflet mechanical heart valve in the mitral position,” *Ann. Biomed. Eng.* **42**,  
849 1668–1680 (2014).
- 850 Daniel, T. L. and Combes, S. A., “Flexible wings and fins: Bending by inertial or  
851 fluid-dynamic forces?,” *Integr. Comp. Biol.* **42**, 1044–1049 (2002).
- 852 Eloy, C., Souilliez, C., and Schouveiler, L., “Flutter of a rectangular plate,” *J. Fluids*  
853 *Struct.* **23**, 904–919 (2007).
- 854 Goldstein, D., Handler, R., and Sirovich, L., “Modeling a no-slip flow boundary  
855 with an external force field,” *J. Comput. Phys.* **105**, 354–366 (1993).
- 856 Hajati, Z., Moghanlou, F. S., Vajdi, M., Razavi, S. E., and Matin, S., “Fluid-struc-  
857 ture interaction of blood flow around a vein valve,” *Bioimpacts* **10**(3), 169–175  
858 (2020).
- 859 Huang, W.-X., Shin, S. J., and Sung, H. J., “Simulation of flexible filaments in a  
860 uniform flow by the immersed boundary method,” *J. Comput. Phys.* **226**,  
861 2206–2228 (2007).
- 862 Huang, W.-X., and Sung, H. J., “An immersed boundary method for fluid-flexible  
863 structure interaction,” *Comput. Methods Appl. Mech. Eng.* **198**, 2650–2661  
864 (2009).
- 865 Khan, M. W. S., and Ali, N., “Theoretical analysis of thermal entrance problem  
866 for blood flow: An extension of classical Graetz problem for Casson fluid model

using generalized orthogonality relations,” *Int. Commun. Heat Mass Transfer*. **867**  
**109**, 104314 (2019). **868**

Khan, M. W. S., Ali, N., and Bég, O. A., “Thermal entrance problem for blood  
869 flow inside an axisymmetric tube: The classical Graetz problem extended for  
870 Quemanda’s bio-rheological fluid with axial conduction,” *Proc. Inst. Mech.*  
871 *Eng.* **H 236**(6), 848–859 (2022). **872**

Khan, M. W. S., Asghar, Z., Ali, N., and Shatanawi, W., “Thermal entry problem  
873 for Vócadlo fluid model bounded within passive tube and channel with axial  
874 conduction and viscous dissipation: A Graetz-Nusselt problem,” *Chin. J. Phys.*  
875 **81**, 219–232 (2023a). **876**

Khan, M. W. S., Asghar, Z., and Hafeez, A., “Graetz problem for the Casson fluid  
877 model with prescribed heat flux in a circular duct,” *Eur. Phys. J. Spec. Top.* **■**,  
878 ■ (2023b). **879**

Kim, K., Baek, S.-J., and Sung, H. J., “An implicit velocity decoupling procedure  
880 for the incompressible Navier–Stokes equations,” *Numer. Methods Fluids* **38**,  
881 125–138 (2002). **882**

Kim, Y. and Peskin, C. S., “Penalty immersed boundary method for an elastic  
883 boundary with mass,” *Phys. Fluids* **19**, 053103 (2007). **884**

Lantz, J., Bäck, S., Carlhäll, C.-J., Bolger, A., Persson, A., Karlsson, M., and  
885 Ebbers, T., “Impact of prosthetic mitral valve orientation of the ventricular flow  
886 field: Comparison using patient-specific computational fluid dynamics,”  
887 *J. Biomech.* **116**, 110209 (2021). **888**

Le, T. B. and Sotiropoulos, F., “Fluid-structure interaction of an aortic valve pros-  
889 thesis driven by an animated left ventricle,” *J. Comput. Phys.* **244**, 41–62  
890 (2013). **891**

Lee, J. B., Park, S. G., and Sung, H. J., “Heat transfer enhancement by asymmetri-  
892 cally clamped flexible flags in a channel flow,” *Int. J. Heat Mass Transfer* **116**,  
893 1003–1015 (2018). **894**

Park, S. G. and Sung, H. J., “Hydrodynamics of flexible fins propelled in tandem,  
895 diagonal, triangular and diamond configurations,” *J. Fluid Mech.* **840**, 154–189  
896 (2018). **897**

Peskin, C. S., “The immersed boundary method,” *Acta Numer.* **11**, 479–517  
898 (2002). **899**

Pierrakos, O. and Vlachos, P. P., “The effect of vortex formation on left ventricu-  
900 lar filling and mitral valve efficiency,” *J. Biomech. Eng.* **128**, 527–539 (2006). **901**

Querzoli, G., Fortini, S., and Cenedese, A., “Effect of the prosthetic mitral valve  
902 on vortex dynamics and turbulence of the left ventricular flow,” *Phys. Fluids*  
903 **22**, 041901 (2010). **904**

Ryu, J. and Sung, H. J., “Intermittent locomotion of a self-propelled plate,” *Phys.*  
905 *Fluids* **31**, 111902 (2019). **906**

Shin, S. J., Huang, W.-X., and Sung, H. J., “Assessment of regularized delta func-  
907 tions and feedback forcing schemes for an immersed boundary method,” *Int. J.*  
908 *Numer. Methods Fluids* **58**, 263–286 (2008). **909**

Sotiropoulos, F., Le, T. B., and Gilmanov, A., “Fluid mechanics of heart valves  
910 and their replacements,” *Annu. Rev. Fluid Mech.* **48**, 259–283 (2016). **911**

Su, B., Wang, X., Kabinejadian, F., Chin, C., Le, T. T., and Zhang, J.-M., “Effect of  
912 left atrium on intraventricular flow in numerical simulation,” *Comput. Biol.*  
913 *Med.* **106**, 46–53 (2019). **914**

Wang, J. S., Gau, Q., Wei, R. J., and Wang, J. J., “Experimental study on the effect  
915 of an artificial cardiac valve on left ventricular flow,” *Exp. Fluids* **58**, 126  
916 (2017). **917**

Wang, S., Ryu, J., Yang, J., Chen, Y., He, G.-Q., and Sung, H. J., “Vertically  
918 clamped flexible flags in a Poiseuille flow,” *Phys. Fluids* **32**, 031902 (2020). **919**

Watton, P. N., Luo, X. Y., Yin, M., Bernacca, G. M., and Wheatley, D. J., “Effect  
920 of ventricle motion on the dynamic behavior of chorded mitral valves,” *J. Fluids*  
921 *Struct.* **24**, 58–74 (2008). **922**

Yang, J., Chen, Y., Zhang, J.-D., Huang, W.-X., and Sung, H. J., “A self-propelled  
923 flexible plate with a keel-like structure,” *Phys. Fluids* **33**, 031902 (2021). **924**

Yeh, P. D., and Alexeev, A., “Free swimming of an elastic plate plunging at low  
925 Reynolds number,” *Phys. Fluids* **26**, 053604 (2014). **926**

Zhang, K., Jeronimo, M. D., and Rival, D. E., “Lagrangian method to simulta-  
927 neously characterize transport behavior of liquid and solid phases: A feasibility  
928 study in a confined vortex ring,” *Exp. Fluids* **60**, 160 (2019). **929**

Zhang, K. and Rival, D. E., “On the dynamics of unconfined and confined vortex  
930 rings in dense suspensions,” *J. Fluid Mech.* **902**, A6 (2020). **931**

AQ5

AQ3

AQ4